SCIENTIFIC REPORTS
nature research

OPEN

Evolution of large area TiS_2-TiO_2 heterostructures and S-doped TiO_2 nano-sheets on titanium foils

S. Ahmad Etghani, E. Ansari & S. Mohajerzadeh*

We report a novel and facile method to synthesize sulfur-doped titanium oxide sheets and realize TiS_2-TiO_2 heterostructures by means of a sequential sulfurization and oxidation step in a dual-zone chemical vapor deposition furnace. The inclusion of chlorine and argon gases during the growth of such titanium-based compounds plays a critical role in the formation of desired geometries and crystalline structures. These heterostructures possess nano-whisker and nanosheet configurations, controlled by adjusting the growth parameters such as temperature, carrier gas and the sequencing between different steps of the growth. The evolution of these complex heterostructures has been investigated using Raman spectroscopy and EDS characterization. The presence of chlorine gas during the growth results in local TiS_2 formation as well as faceted growth of TiO_2 nanosheets through anatase to rutile phase change prohibition. The electron microscopy (TEM) images and diffraction pattern (SAED) characterization reveal the crystallinity and layered nature of grown structures, further demonstrating the 2D characteristics of S-doped nanosheets. The evolution of TiO_2 on TiS_2 heterostructures has also has been verified using XPS analysis. These highly featured nanostructures are suitable candidates to enhance the photocatalytic behavior of TiO_2 nanostructures.

Transition Metal oxides (TMOs) with their versatility in crystallographic structures and solid-state properties are emerging materials for both research institutes and industrial enterprises. In the meantime, titanium dioxide possesses a large part of this research activity and investment enthusiasm. Although a great research stream is active on photocatalytic behaviors and optical applications of TiO_2 polymorphs (Rutile, Anatase and Brookite)[1,2], they have shown diverse physical and chemical properties, which make them a desirable candidate for applications such as food additives[3], bioactive coatings[4], drug delivery agents[5] and also in flexible electronics[6] in their nano-shaped forms.

The synthesis of TiO_2 nanostructures in the forms of 1D features such as nanoribbons[7], nanowires[8] and nanotubes[9] and 2D structures like nano-sheets[10] as well as 0D nanoparticles[11] has introduced new possibilities in their fields of applications. TiO_2 nanostructures show enhancement in their photocatalytic activity (PCA) compared to their bulk counterparts[12]. Moreover, the higher surface to volume ratio of nanostructures brings a broader active field to absorb the incident ultra-violet (UV) spectra and their coupling with confined structures such as gold disks[13]. Along with the superior characteristics gained through size reduction, efforts have been made towards the growth of crystalline structures along with the desired facets due to the unique characteristics of special crystalline planes of TiO_2[14]. In general, a faceted growth results from the minimization of surface energy which reveals surface-dependent features, depending on different Ti-O bonding and oxygen and titanium deficiency in the crystal structure. These dependencies to crystal surface play a dominant role in the anatase phase in which higher photocatalytic activities are expected. Furthermore, a better heterogeneous catalytic performance of {001} faceted grown sheets of the anatase phase of titanium-oxide towards {101} or {100} tailored structures is predicted owing to the presence of five coordinated Ti atoms, leading to higher surface energy[15,16].

The tailored faceted synthesis of TiO_2 has been investigated through both chemical and physical methods such as MOCVD[17], CVD[18], Molecular Beam Epitaxy[19], solvothermal[20] and hydrothermal[21] methods while the two previous ones are the most favorable techniques. Using a capping agent such as Cl^-[22], F^-[23] and SO_4^-[24] and also flow of reactive gases such as chlorine can facilitate the evolution of facets with higher surface energies and higher indexes. The presence of reactive agents can affect the phase transformation of TiO_2 polymorphs during the growth, as they can be classified into promoters and inhibitors of anatase to rutile phase changes[25]. The

Thin Film and Nanoelectronic Lab, School of electrical and computer Eng., University of Tehran, Tehran, Iran. *email: mohajer@ut.ac.ir

inclusion of reactive agents during the growth process can also act as a doping agent in the synthesized materials. The predetermined doping along with their post-growth residues can alter the solid-state properties of the grown structures. Owing to the critical role of TiO_2 nanostructures in photocatalytic applications, the purpose of most investigations in this field is the enhancement of photoabsorption efficiency in the prepared samples and therefore, both metallic (i.e., Fe^{3+} and Cu^{2+})[26] and nonmetallic (i.e., N, P, C and S) species[27,28] are deployed. Ion implantation as a novel technique for doping of TiO_2 nanostructures has been introduced by Li *et al.*[29]. Moreover, Song *et al.*[30] have implemented the "Midas Touch" transformation through ion implantation of carbon and nitrogen dopants in the pristine TiO_2 structures and enhanced the photoelectrical properties of the material.

Among the additives and dopants, sulfur as a non-metallic dopant has grasped the interest of researchers due to its contribution in adjusting TiO_2 bandgap, as a result of sulfur substitution into oxygen sites of the lattice[31]. In order to achieve sulfurized TiO_2 structures, different growth and doping techniques have been employed ranging from wet chemistry solvothermal[32], hydrothermal[33] and sol-gel synthesis[34] to H_2S treatment of TiO_2 particles[35]. While CVD-based growth techniques have been widely employed to prepare S-doped samples[33], the oxidative annealing of TiS_2 films is known as a conventional method to achieve S-doped TiO_2 nanostructures[28]. Jing *et al.*[36] synthesized anatase TiO_2 nanosheets through electrochemical exfoliation of TiS_2 by lithium intercalation and subsequent sonication and centrifuging. The TiO_2 nanosheets were then derived by a hydrothermal process in O_2 purged solution.

In this work, 2D layered crystalline S-doped TiO_2 nanosheets are grown on titanium substrates through a dual-zone CVD synthesis technique. A sequential procedure of the growth is implemented by sulfurization and subsequent oxidation in Ar and different Ar/Cl gas environments. The effect of chlorine gas on the growth mechanism has been investigated by changing the Ar:Cl gas ratios. The CVD furnace is equipped with a peripheral in-process load/unload apparatus for better monitoring and controlling the growth. The fabricated nanostructures have been thoroughly examined utilizing EDX, SEM, XPS, TEM, SAED, and Raman spectroscopy techniques. TiO_2 surfaces covered with nanosheets were analyzed for the potential photocatalytic characteristics through temporal UV-Visible spectroscopic characterization of photodegradation in a Methylene Blue (MB) aqueous solution. The reaction kinetics of the photocatalytic process in nanostructured TiO_2 samples have been studied using pseudo-first and second-order models.

Materials and Methods

The experiment is conducted in a dual-zone CVD tube furnace (depicted in Scheme 1a) in the presence of Ar/O_2 gas flow. The furnace is evacuated with the aids of a mechanical rotary pump down to a base pressure of 20 mTorr for the initiation of the growth process. The sublimation zone of the quartz tube is located at one end of the tube to heat up the sulfur reservoir and to provide the necessary sulfur vapor precursor in the reactor. This zone is heated up to 250 °C with a slow rate of 20 °C/min and feeds the system with sulfur vapor, sublimated from 12 grams of S-powder. The hot zone maintains a higher temperature of 650 °C to host the growth and the TiO_2 nanosheets are grown on a pre-cleaned titanium foil mounted on a quartz plate in this hot zone. Titanium foils (Good-Fellow, 99.6 + % purity) are used as the growth substrate and they are prepared through a preliminary cleaning step by immersing in a dilute HF (8:1 DI Water: HF) solution. Besides removing the native oxide layer formed on the Ti surface, a rather corrosive reaction between hydrofluoric acid (HF) and titanium increases the roughness of the foil surface to improve the growth and capturing probability of the inlet gases.

To achieve vertically-grown few-layered TiO_2 nanosheets, the pre-cleaned Ti foils experience a sequential process (Scheme 1b). The synthesis begins with elevating the hot zone temperature to 650 °C in an Ar ambient with a gas flow of 15 sccm. After the initial pumping cycle, and to increase the pressure of the ambient gas and enrich the gas stream with sulfur, the pumping of the CVD reactor proceeds through the bypass evacuation mode which increases the furnace pressure up to 2 Torr (in the presence of Ar gas). This condition increases the presence of gaseous reactants on the surface of the Ti substrate. At this stage and by reaching the desired temperature in the hot zone, the pressure is maintained at the desired value and the sublimation of sulfur powder is started. This process is taken place in the flow of Ar/O_2 gas with 15 scmm flow rates. The mixture of sulfur vapor and O_2 gas plays a critical reactant role for the synthesis of TiS_2 and $TiS_{2-x}O_x$ on the surface of the Ti substrate. After the termination of the sulfurization process, the flow of Ar/O_2 gas mixture is maintained. The growth of TiO_2 nanosheets mainly proceeds at this oxidation step when the cooling of the sublimation zone progresses to reduce the presence of sulfur remnants on the surface of the sample. This condition is kept for one hour and accompanied by another cool-down step of the main hot zone of the furnace.

It has been shown[37] that the presence of chlorine gas or chloride compounds during the growth process of titanium sulfide nanostructures can play an effective role because of the intermediary reaction between Ti and Cl species. Thereupon, the experiments are carried out by various Ar/Cl gas flows along with Ar/O_2 mixture during the growth step. Two different mixtures of argon/chlorine gases (99.5/0.5 and 98/2) were used to trace the impact of the reactive agents in the nanostructure formation. To investigate the growth process in each step we have equipped the CVD apparatus with a loading rod which can transfer the sample from the hot zone to the cold zone in a smooth and rapid manner. Special care should be taken into account to ensure the vacuum is not affected during loading/unloading the sample during this transfer rod.

Results and Discussion

Synthetization of S-doped TiO_2 nanostructures was taken place in a sequential manner through sulfurization and oxidation steps which led to the formation of a nonstoichiometric titanium oxysulfide film as a groundwork for the growth of TiO_2 sheets. The formation of free-standing nanostructures at the presence of three gases is considered as a backing substrate for the evolution of TiO_2 sheets and whiskers. The SEM images of TiO_2 nanosheets grown through the aforementioned procedure in the Ar/O_2 gas flow are shown in Fig. 1a. TiO_2 nano-whiskers have emerged from a bulky substrate that resembles condensing of 2D surfaces which form a thick uniform film.

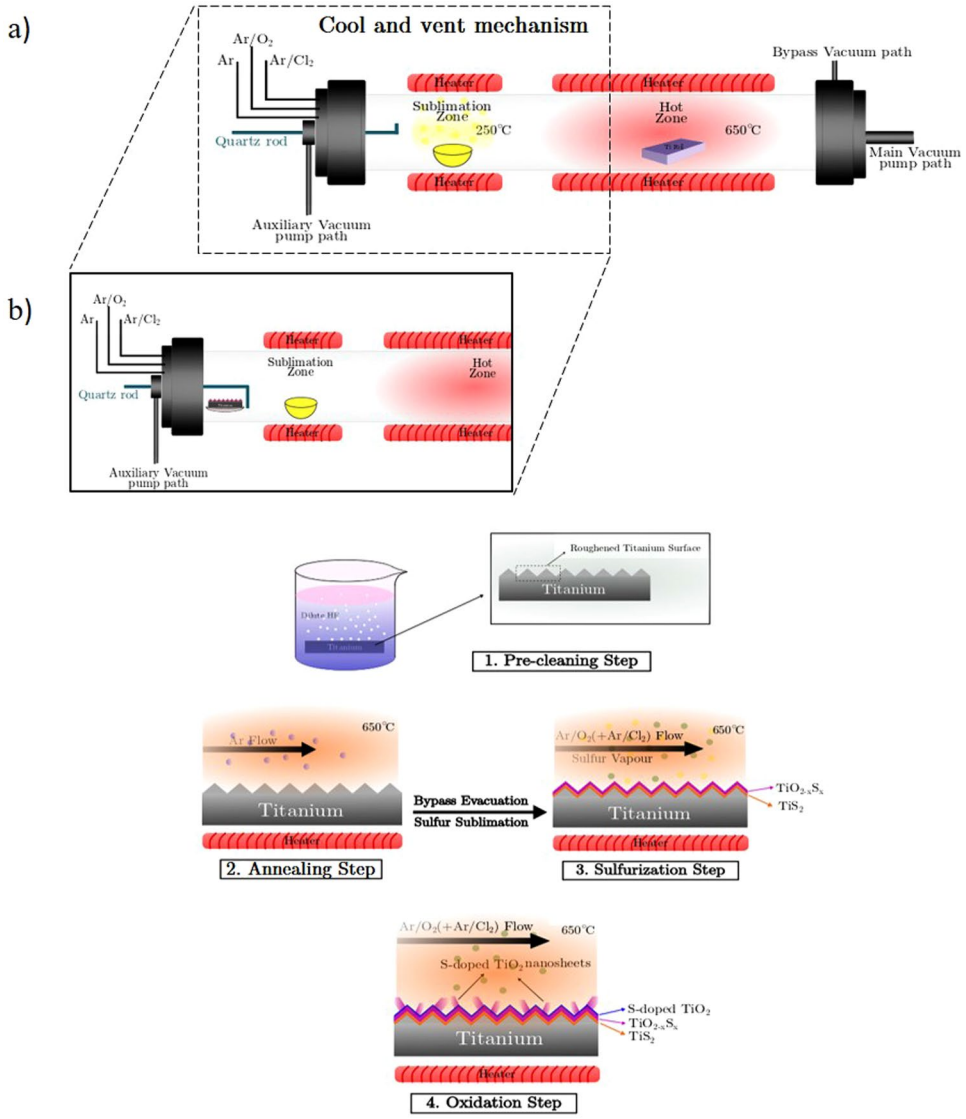

Scheme 1. Schematics of growth apparatus and the proposed growth mechanism. (**a**) The enhanced CVD furnace for the growth of S-doped TiO_2 nanostructures (dashed box depicts the cool and vent mechanism appended to this system for rapid sample pull-out). (**b**) The sequential growth process flow; surface roughening using HF solution, followed by annealing at 650 °C and sulfur exposure at the same temperature. The initial layer would be TiS_2 whereas the top layer would turn into an oxidized layer during the oxidation step, forming heterostructures. S-doped TiO_2 nanosheets are synthesized through the oxidation and subsequent cooling step.

The thicker layers are detached on the upper surfaces and consequently, TiO_2 nanostructures are flourished from these bulky and rough grains.

To enhance the sulfurization of titanium foils, the chlorine gas (Ar/Cl) is supplied into the growth reactor during this step as well as the oxidation one. The presence of chloride precursors leads to a significant improvement in the formation of titanium sulfide compounds. Introducing Ar/Cl (98:2) to the sulfurization step has led to a uniform growth of TiS_2 nanosheets (Fig. 1b) and suppressed the formation of TiO_2 films and nanostructures. The nanosheets synthesized in the chlorine-rich process have been studied using Raman spectroscopy and the corresponding data are depicted in Fig. 1c, where a sharp peak at 336 cm^{-1} corroborates the evolution of TiS_2 nanosheets on the titanium surface.

The cease in the growth of titanium oxide and subsequent formation of TiS_2 instead of TiO_2 can be related to a probable reaction that is taking place between titanium foil and chlorine gas at an elevated temperature, which results in the regional formation of $TiCl_4$ compounds on the Ti substrate. This hypothesis is based on the fact that metallic titanium shows a great tendency for the chlorination at temperatures about 300 °C which has been defined through thermodynamic states of reaction[38]. This reaction results in the gaseous $TiCl_4$ byproduct through the reaction introduced in Eq. 1.

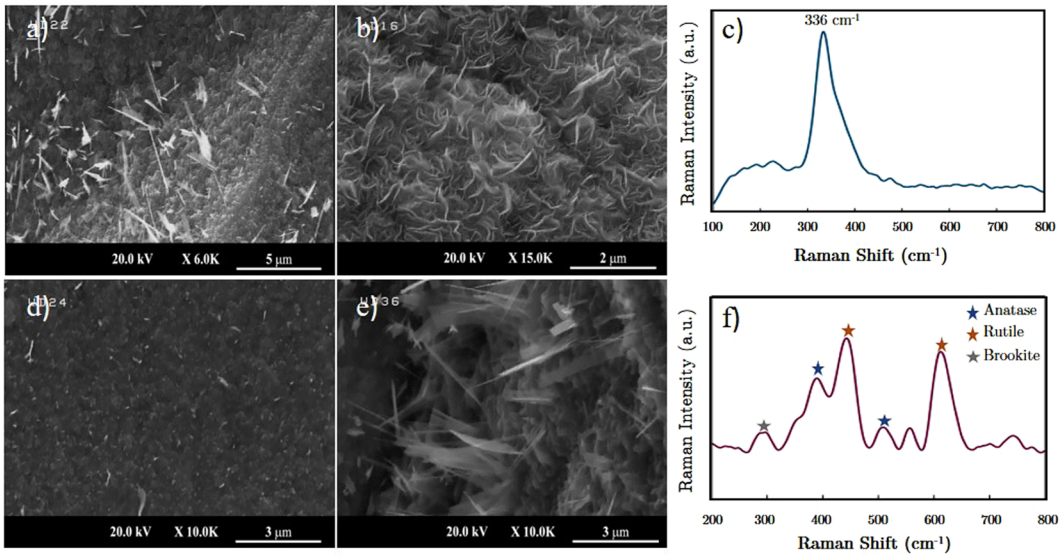

Figure 1. SEM images and corresponding Raman results of grown structures on pre-cleaned titanium substrates. (**a**) TiO_2 nanowhiskers grown in Ar-Ar/O_2 environment, (**b**) growth of TiS_2 nanosheets in Ar/Cl_2 (2%)-Ar/O_2 environment, (**c**) Raman spectroscopy of (**b**), (**d**) Sample experiencing abrupt extraction by means of cool and vent apparatus after sulfurization, (**e**) The evolution of 3D sheets in the growth environment of Ar/Cl_2 (0.5%)-Ar/O_2 gas streams. (**f**) The observed Raman spectroscopy of (**e**), identifying the presence of Anatase, Rutile and Brookite phases of TiO_2 structures.

$$Ti_{(s)} + 2Cl_{2(g)} = TiCl_{4(g)} \quad (1)$$

It is worth mentioning that the gaseous $TiCl_4$ is widely used in producing titanium oxide[39] and sulfide[40] nanostructures. In the growth mechanism proposed in Scheme 1, the presence of sulfur vapor and oxygen gas in the sulfurization and further oxidation steps have made a competition role of $TiCl_4$ as an intermediator between TiS_2 and TiO_2 nanostructure formation. It is well-known that the byproducts of the chlorine residues are easily removed from the surface of the sample and as a result, the presence of chloride compounds are not observed after the growth is complete[41]. The gaseous titanium tetrachloride is widely used as precursor in the growth of TiS_2 nanostructures and its reaction with H_2S gas in MOCVD furnaces has also been a favorite approach to arrive at different TiS_2 films[42]. The massive TiS_2 nanosheet formation in the chlorine-rich environment can be correlated to $TiCl_4$ formation in the growth chamber and its further reaction with sulfur vapor generated through the sulfur sublimation. The presence of Ar/Cl mixture and dominancy of chloride compound formation suppresses the oxidation step and minimizes the undesired transition from TiS_2 to TiO_2 structures.

The amount of chlorine gas in the 2% Ar/Cl mixture is high enough to suppress the oxidation step and lead to desired TiS_2 structures. In order to achieve TiO_2 nanostructures, the chlorine gas ratio has been reduced to 0.5% to allow the reaction between titanium sulfide counterparts with oxygen, leading to TiO_2 formation. The SEM image of titanium dioxide nanostructures formed in chlorine and oxygen environment is shown in Fig. 1e. The Raman spectra of this sample have been displayed in Fig. 1f, which depicts the presence of TiO_2 phase in the nanostructured substrate and will be thoroughly studied in the following sections. The enhanced growth of nanostructures on the Ti substrate reveals the effectiveness of chlorine agent in the process. The role of chlorine gas in forming $TiCl_4$ regions has improved the probability of local TiS_2 formation by preparing a favorable growth substrate. The oxidation process coming along with this sulfide compound growth can lead to transitions to titanium oxide and to prepare an appropriate field of growth for TiO_2 nanostructures and eventual TiO_2/TiS_2 heterostructures.

To grasp a better insight about the grown structures, the upper surfaces of the samples are scratched off and the electron microscopy has been carried out on the peeled samples. The cross-sectional SEM image of the cleaved substrate revealed that the aforementioned sequential procedure has led to the growth of highly layered structures on the Ti substrate (Fig. 2) where highly dense sheets are created on top of each other. The EDX mapping reveals the nature of each layer and as seen in the sulfur elemental map of the sample where the lower layers are sulfur-rich, indicating the TiS_2 sheets formation and the top features are more oxygen-rich, corresponding to TiO_2 structures. The middle layer between the TiS_2 nanosheets and the TiO_2 layer synthesized during the oxidation layer has been formed due to possible strains during the growth of structures with different crystalline characteristics and is a sulfur-deficient TiS_2 layer ($TiS_{2-x}O_x$). This section has been synthesized in the sulfurization step in the presence of oxygen flow.

The presence of chlorine in the growth environment with a relative percentage of 2% seems to be critical in achieving such titanium-based heterostructures. The percentage of sulfur compound experience a noticeable diminution at upper layers. The innermost layer shows sulfur-rich layers of TiS_2 sheets which were experienced

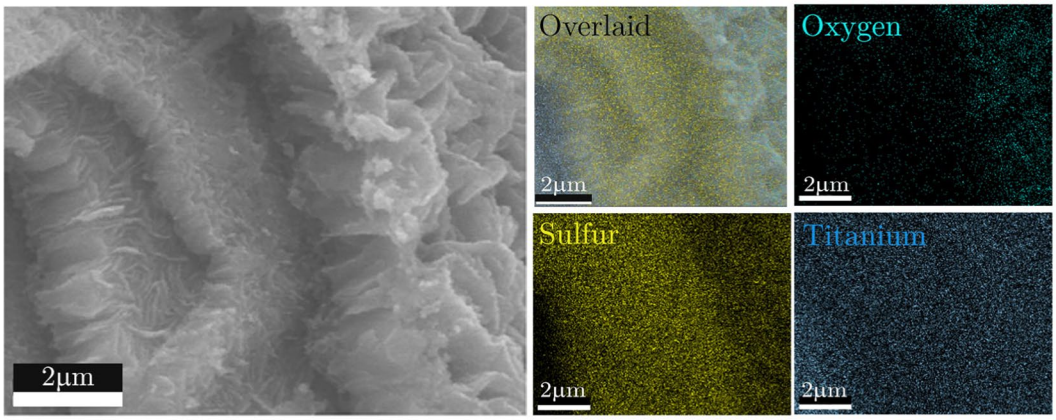

Figure 2. The elemental analysis (EDX) mapping of layered nanostructures grown on a pre-cleaned titanium substrate in Ar/Cl_2 (0.5%). The highly layered structure is evident from the SEM image on the left side. While Ti is observed in all regions, the oxygen concentration is observed more in the upper layers, whereas sulfur shows a higher concentration at the lower layers.

a further EDX analysis presented in Fig. S1 by scotch tape transfer of grown layers on a silicon-based substrate. The topmost layer formed in the capacious nanosheets demonstrates a substituted behavior in the incorporation of oxygen atoms inside their structure. The excess of oxygen atoms can be traced by the EDX mapping of this element on the sample. The evolution of sulfur and oxygen atoms indicates that the upper layer has undergone an oxidation step where sulfide structures are transformed into titanium oxide form.

From the results of EDX analysis and Raman spectroscopy, it can be deduced that the TiO_2 substrate on which TiO_2 whiskers are grown has experienced a transition from TiS_2 to TiO_2 structures and a further phase transition from anatase to rutile, controlled mainly by the chlorine agent and the growth temperature. The transition of Titanium Sulfide to their titanium oxide counterpart and establishment of the growth in the oxidation step has provided an appropriate field of growth for S-doped TiO_2 nanosheets. To evaluate this point, a manipulating apparatus is added to the CVD reactor which allows pulling out the samples from the hot zone after sulfurization step (depicted in Scheme 1a) in a modest time. A curved neck quartz rod is used to drag the sample's boat towards the cold zone smoothly and after a period of cooling of 15 minutes. This cool and vent mechanism is an important step to avoid instantaneous exposure to air and oxygen. The SEM image of the samples presented in Fig. 1d shows that the growth of TiO_2 whiskers was not established which suggests that the growth of nanostructures is performed mostly during the oxidation and cooling step.

The shifts in the Raman peaks depicted in Fig. 1f, sheds light on the presence of both two stable phases of TiO_2 as anatase and rutile phases, on the cover layer of the synthesized structure. The anatase TiO_2 structure has six vibrational modes as $\Gamma = A_{1g} + 2B_{1g} + 3E_g$ signals are Raman active modes whereas four Raman active modes of $\Gamma = A_{1g} + B_{1g} + B_{2g} + E_g$ are conceivable in the rutile phase. The Raman peaks of stable phases of TiO_2 can be found in authentic papers[43,44]. The Raman spectra of the top layer of the sample shows five distinct peaks at 392, 447, 514, 561 and 614 cm^{-1} wavenumbers. The peaks located at 392 and 514 cm^{-1} wavenumbers can be interpreted as B_{1g} and B_{1g}, A_{1g} modes of the Anatase phase. The dominant peaks of Raman analysis are devoted to 447 cm^{-1} and 614 cm^{-1} wavenumbers which are consistent with signals reported for rutile phase TiO_2. The predominance of rutile TiO_2 peaks has the relevance with the growth temperature of samples (650 °C) and the fact that TiO_2 nanostructures experience a phase transformation from anatase to rutile configuration in the temperatures ranging from 600 °C to 1200 °C. A disjoint peak has appeared in the Raman spectra of the TiO_2 samples at 561 cm^{-1} wavenumber which can be referred to as S_3 molecules of sulfur, formed during the oxidation step or residues remained during the cooling process[45]. Also another peak in 288 cm^{-1} can be detected which can be attributed to the Brookite phase TiO_2[46].

Although the anatase-rutile transition can be traced in the growth procedure, its effect on the formation of TiO_2 nano-whiskers needs to be investigated. In order to understand this effect, two samples with different Anatase/rutile ratios were prepared by displacement of Ti substrate positions with respect to each other into the hot zone of the furnace. The resulted samples show slightly different surface morphology which led to variation in the number of whiskers grown on them as collected in Fig. 3. The nanostructures covering each sample propose a dissimilarity in the phase of the TiO_2 substrate. The shifts in the Raman spectra correspond to various shifts which belong to highly complex structures. It is observed that the ratio of Raman peaks especially at 398 cm^{-1} and 147 cm^{-1} wavenumbers (anatase phase) to the peaks at 447 and 619 cm^{-1} wavenumbers (pertaining to rutile phase) is higher in the densified whisker grown sample which suggests that the anatase phase is a better field of growth for the vertically grown nanostructures.

In order to determine the anatase/rutile ratio in two samples, we have employed the formalism proposed by Clegg *et al.*[47] in which the 147 cm^{-1} peak of Anatase phase and the 614 cm^{-1} peak of rutile phase were candidates for the representation of their content in the Raman spectroscopy result. As the appearance of the 147 cm^{-1} peak is very sensitive to the presence of anatase content, this methodology can be used for a better quantitative

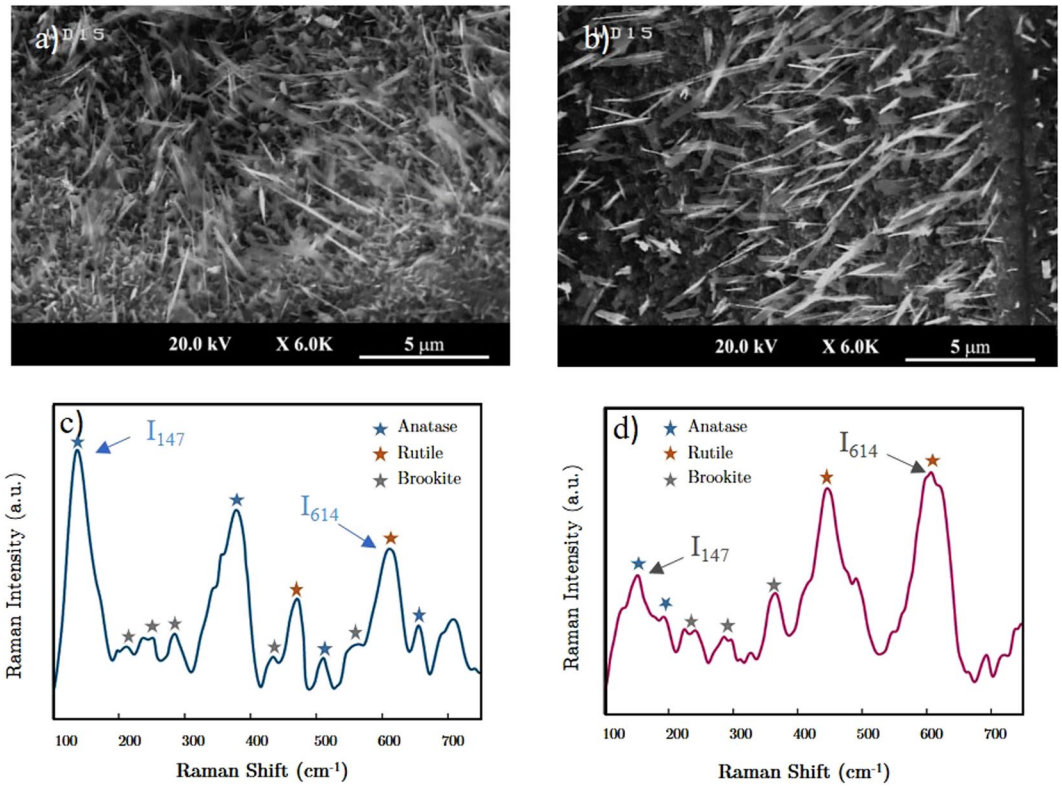

Figure 3. Effect of dominancy of each TiO_2 stable phase in the amount of synthesized nanowhiskers coverage on the Titanium substrate. (**a**) SEM image of whiskers grown on higher anatase to rutile phase TiO_2 films, (**b**) Raman spectroscopy of sample (**a**), (**c**) SEM image of whiskers grown on higher rutile to anatase phase TiO_2 films, (**d**) Raman spectroscopy of sample (**c**). The ratio of Raman peaks at 614 cm^{-1} to 417 cm^{-1} wavenumbers can be considered as a measure to obtain a quantitative insight about this phase transition.

interpretation[48]. The anatase/rutile ratio is measured by means of dividing the intensity of Raman peaks at 147 cm^{-1} and 614 cm^{-1} and derived from the following equation;

$$R = \frac{Anatase\ content}{Rutile\ content} = \frac{I_{147}}{I_{614}} \quad (2)$$

The value of R, calculated for the sample with higher anatase content coverage (Fig. 3c) is 1.46 and this value decreases to 0.44 for the other sample which its Raman analysis is depicted in Fig. 3b. This observation leads us to conclude that the faceted TiO_2 nanosheets are the consequence of anatase phase TiO_2 formation on the layered film and anatase-rutile phase transformation is an unfavorable process which can terminate the growth procedure. This result highlights the role of chlorine gas in the growth process. The fact that the chlorine reactant is an inhibitor of anatase to rutile phase transition[49] beside the aforementioned results proposes that the densified growth in the presence of Cl gas is a consequence of phase change prohibition enforced by the chlorine agent. This effect besides the intermediary role of chlorine in the formation of TiS_2 sub-layers facilitates the growth of faceted structures.

The nano-whiskers were analyzed by energy dispersive spectroscopy (EDS) mapping to characterize the corresponding constituent elements. Figure 4a shows the presence of titanium, oxygen and also sulfur components in the sample. The mapping of each element elucidates the sulfur doping into titanium oxide nanostructures. A more exact examination of the sulfur portion in the structure can be achieved by line scanning of the whisker structures. The line-scan, provided in part (b), reveals the presence of sulfur on the scanned region and the O/Ti ratio below 2. The oxygen-deficient TiO_2 nano-whiskers have been doped during the growth process by sulfur components which were presented either in the oxidation step of titanium sulfide substrate and its transition to titanium oxide or through their sulfur-rich seeds of growth.

Figure 4c shows high-resolution XPS results of the TiO_2 sample. From the line-scanning EDX analysis presented in part (b), the contribution of sulfur species on the surface film formed on the fully processed samples after the oxidation step is minor and the XPS analysis can further confirm this conclusion. As depicted in S 2p XPS spectrum, although the measured peaks are weak, they are consistent with the reported peaks for sulfur ionic states in S-doped TiO_2 and TiS_2 films. By means of XPS measurements, the presence of S^{2-}, S^{4+} and S^{6+} anionic and cationic species has been shown in the TiO_2 samples prepared either by oxidation of TiS_2 films[50] or utilizing sulfur-based precursors during the growth process[51]. As stated by Han *et al.*[52], sulfur S 2p peaks can be classified into two regions with binding energies of (I): 160–163 eV which present the S^{2-} anionic states contributing in

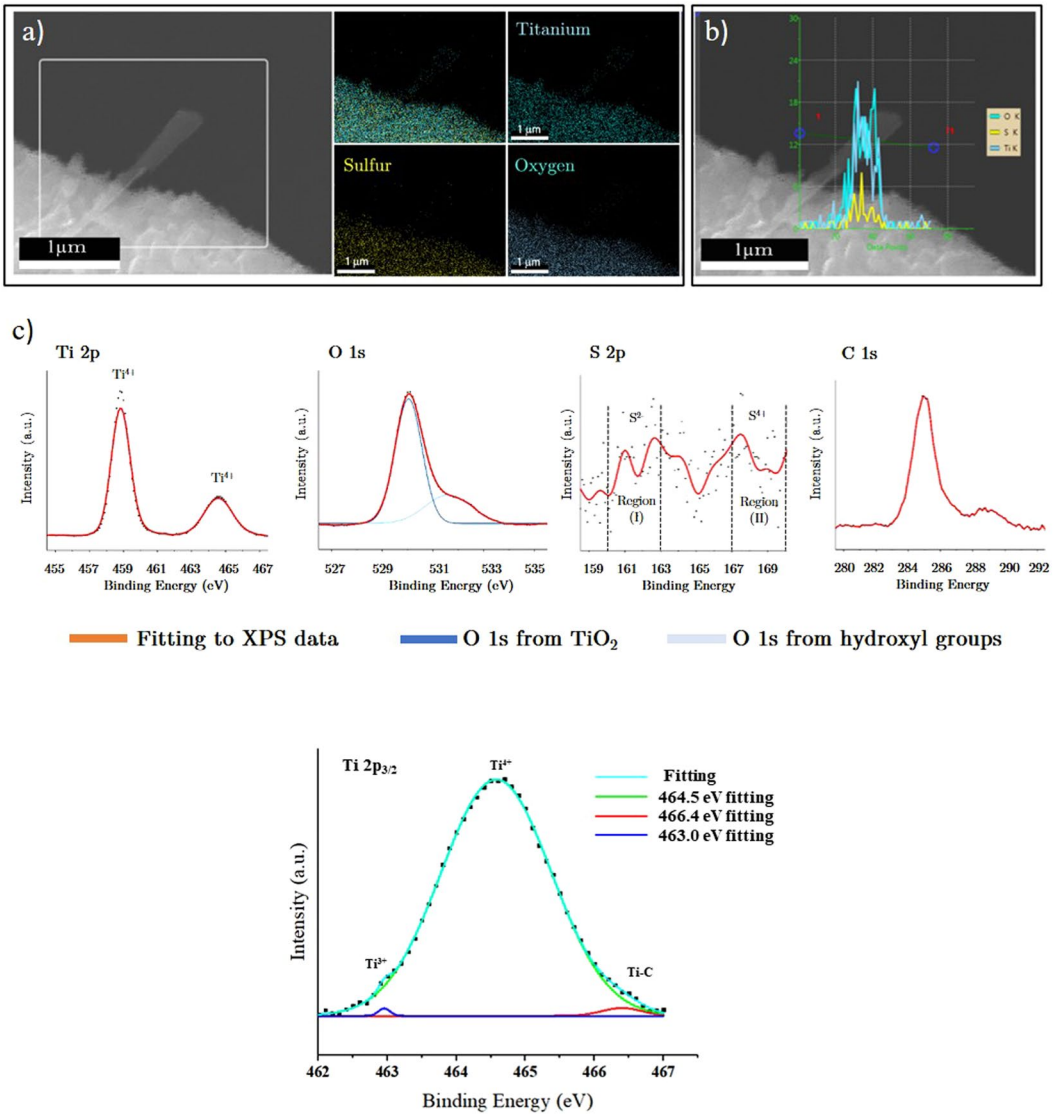

Figure 4. The EDX analysis and high-resolution XPS spectra measurement of S-doped TiO_2 samples. (**a**) EDX mapping of titanium, sulfur and oxygen elements on nanowhiskers, (**b**) line scanning of single nanowhisker grown on TiO_2 substrate. (**c**) The XPS analysis of nanowhiskers; the evolution of Ti-O bonds is observed from O1s peak. Since the XPS shows the very top surfaces of the sample, the presence of sulfur is less strong, although three regions of S bonds are observed in this figure. (**d**) The deconvoluted Ti $2p_{3/2}$ peaks which is assumed to be due to Ti^{3+} bonds.

the Ti-S bonds and replaced with the O^{2-} species, suggesting the substitution of oxygen atoms with sulfur[53]. The second region is region (II) which lays between 167 and 170 eV. This region is referred to as S^{4+} and S^{6+} cationic species replacing the Ti^{4+} states in the TiO_2 crystal[54]. They can also be made from S–O and S=O bonds[55] originated from the formation of SO_4^{2-} or SO_3^{2-} on the sample surface. The synthesized sample shows S 2p peaks in both regions. In the first region two peaks with binding energies of 162.6 and 160.9 eV were found which have good consistency with the S $2p_{1/2}$ and S $2p_{3/2}$ in the titanium and sulfur bonding in TiS_2 compounds[56] and express the replacement of S^{2-} anions in O^{2-} sites in the TiO_2 lattice and the formation of slight doping in the sample. The other sulfur peak is found in the second region around 167.4 eV which represents the S^{4+} cationic species[57]. This evidence suggests that sulfur acts as both cationic and anionic doping in the synthesized sample through replacement with O^{2-} as well as Ti^{4+} atomic states. The XPS analysis does not show an indication of S^{6+} and SO^{4-} species.

The results obtained for titanium species indicate the significant peaks of Ti^{4+} in TiO_2 with binding energies of 458.7 and 464.5 eV, which relates to Ti $2p_{3/2}$ and Ti $2p_{1/2}$ components[58]. Although the peaks are slightly shifted toward lower energies which can be related to the presence of sulfur species in the structure[51], the predominance of TiO_2 related Ti 2p peaks and the lack of TiS_2 ones do not show strong sign of sulfur species. This can be related to the lean doping of sulfur atoms into the structure or the dominancy of S^{4+} in the doping profile.

Having a closer inspection of the Ti $2p_{3/2}$ peak, two marginal minor peaks can be extracted from the shoulder of the spectra. The extracted peaks have been depicted in Fig. 4d with binding energies of 463 eV and 466.4 eV.

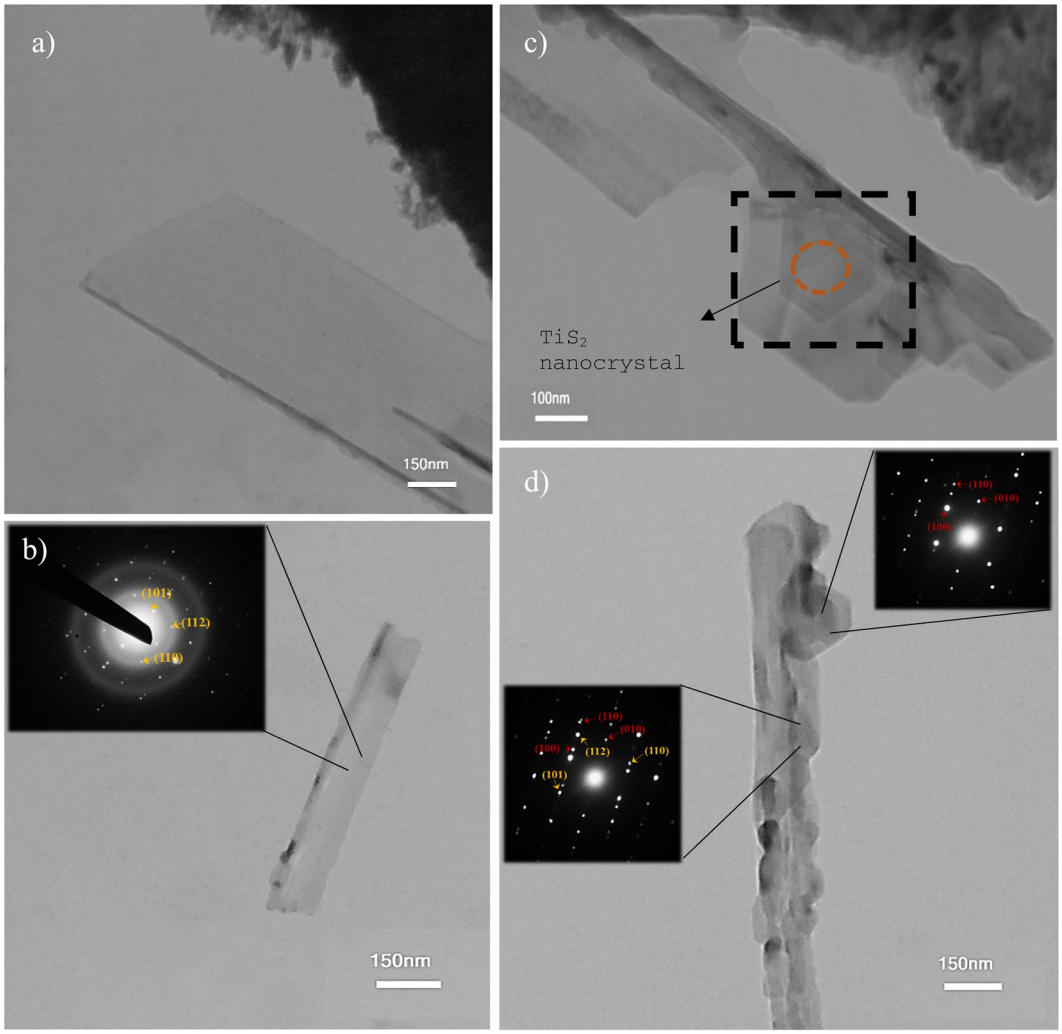

Figure 5. Collection of TEM images from various TiS_2/TiO_2 structures. (**a**) Ultrathin S-doped nanowhisker; (**b**) 2D layered nanowhisker, inset: SAED pattern and twinning in the diffraction pattern of nanowhiskers, (**c**) TiS_2 nanocrystal emerged into the 1D structure, (**d**) nanowhiskers with their TiS_2 seeds; insets depict the electron diffraction patterns of TiS_2 nanocrystal and tailored nanowhisker. The green indexes belong to TiO_2, while the red ones belong to TiO_2.

The sharp peak locating at 463 eV with FWHM of 0.17 belongs to the Ti^{3+} state of titanium. During the growth process leading to titanium oxide or sulfide, the presence of oxygen and sulfur in the gas state can dissociate the $TiCl_4$ product to form byproducts such as $TiCl_3$[59] or $TiOCl_2$[60]. The Ti^{3+} states participating in these compounds can be the origin of 463 eV peak. The other peak with a binding energy of 466.4 eV can be attributed to the presence of Ti-C bonding on the sample[61].

The O 1 s spectra of the synthesized sample reconfirms the dominancy of TiO_2 film formation with the 530 eV peak whose energy is in good agreement with the binding energy of titania[62]. As depicted in the XPS graph the spectrum is made with the combination of main TiO_2 peak with the one with binding energy of 531.8 eV. This marginal peak can correspond to the oxygen atoms of hydroxyl groups or sulfate ones[63], in which the hydroxyl formation on the substrate shows a better consistence with the results obtained from sulfur S 2p spectra. The C 1 s spectra is due to contamination and with the peak in 284.9 eV brings a 0.1 eV shift to reach the C-C bonding at 284.8 eV.

The SEM images of synthesized structures show that the nanowhiskers are few-layered materials which are nearly transparent under electron beam exposure. A better inspection of these whiskers has been made using a Philips CM300 transmission electron microscopy, operating at 200 kV. Figure 5 depicts a bright-field TEM image of a whisker where a highly crystalline structure is evident. This image reveals the ultra-thin nature of nano-whiskers which are smoothly folded on their edges (Fig. 5a). The electron diffraction pattern (SAED) from the selected region displays the crystallinity of structures and whiskers. As the anatase TiO_2, acting as the growth substrate for nano-whiskers, has a tetragonal unit-cell ($P4_2/mnm$ space group), its diffraction pattern can be formed in a parallel line configuration. The SAED pattern depicted in the inset of Fig. 5b appeared in a twining form which can be referred to overlaying parallel plane features and demonstrates the layered nature of

nano-whiskers. The analyzed pattern exhibits excellent agreement with the anatase phase TiO_2 nanostructures. The (101), (112) and (110) planes have been identified and indexed in the selected area diffraction patterns in this figure[64].

The sequential growth and the gradual formation of TiO_2 whiskers from TiS_2 layers, studied by means of EDX analysis and Raman characterization. A clear delineation of this growth procedure can be traced in Fig. 5c in which the black dashed part of the TEM image depicts the TiS_2 nanocrystal as the seed inside the nanowhisker. As highlighted with the dashed circle in this image, the hexagonal-shaped nanocrystal has tailored into 1D-shaped layer during the growth procedure which can shed light on the growth mechanism for TiO_2 nanowhisker. The SAED patterns of these merged structures were characterized separately (Fig. 5d) in which the nanocrystal has a hexagonal diffraction pattern and the indexed pattern displays a good agreement to the one presented for TiS_2 nanosheets[65] the TiS_2 nanocrystal is not isolated from the tailored nanowhisker and a heterostructure of stacked nanostructures can be assumed for the region being analyzed. Due to this fact, the neighbor structure has a trace in the pattern which is derived. This companionship can be followed in the SAED pattern of the tailored part of the material. This pattern displays concurrent presence of TiO_2 and TiS_2 planes which correspondingly indexed in the inset of Fig. 5d. This evidence reveals that the evolution of the TiS_2 structures has resulted into the growth of these S-doped nanowhiskers and the desired heterostructure of TiS_2 and TiO_2 nanostructures.

The photocatalytic behavior of nanostructured samples has been investigated by inspecting the degradation of Methylene Blue (MB for short, purchased from Merck) aqueous solution under UV lamp illumination. The photo-catalysis tests were performed with 5 ppm MB solution with a pH level of 8.5, which due to the Point of Zero Charge (PZC) pH level of 6.8 for TiO_2 nanoparticles[66], an electrostatic absorption can be assumed between TiO_2 negatively charged surface and MB dye[67]. The photocatalytic behavior of the TiO_2 samples covered with nanowhiskers was compared with the TiO_2 sample synthesized through 10 min oxidation step and extracted from the furnace by means of cool and vent apparatus depicted previously in Scheme 1 (part a). The reference sample has experienced an abrupt cool and vent mechanism after the primary 10 min oxidation which interrupts the process of nanostructure formation on the TiO_2 surface. To evaluate the mass of covered surface on the samples, the surface of identical substrates peeled off with the aid of scotch tape which resulted in 4 micrograms coverage of synthesized material on the Titanium foil. The samples are constantly stirred in a 10 mL MB solution. All photodegradation tests have been performed under irradiation of 365 nm UV lamp with a power of 160 Watts and for a duration of 140 min. These tests have been performed after 40 minutes of dark adsorption equilibrium, the results of which have been provided in Fig. S2 of supplementary information. Also, the photodegradation of MB without catalysts has been conducted (Fig. S3), which shows a negligible removal of the dyestuff without catalytic reactions.

The absorption spectrum of the degraded solution is presented in Fig. 6a,b for the reference and nanostructured samples, respectively. The UV-Visible characterization depicts the degradation of Methylene Blue dyes concentration through the photocatalytic action; although the complete refinement of aqueous solution shows a slow rate that reveals the fact of catalyst deficiency. A slight, blue-shifted displacement of the absorption peak in both samples was observed which can be referred to the Hypochromic effects occurring in the process of Methylene Blue N-demethylation[68]. The test conducted with higher concentration and volume of dyestuff and its subsequent solution (10 ppm and 20 mL) resulted in different shift values (4 nm for nanostructured sample and 1 nm in the case of reference substrate) in the course of 120 minute degradation time which lights up the interaction between nanowhiskers and contaminant dyes and the role of TiO_2 nanostructures in cleansing MB solution and subsequent reduction and oxidation potential increment[69].

The photocatalytic behavior of samples was evaluated through the calculation of the percentage of dye concentration removal using Eq. 3.

$$\eta(\%) = \frac{C_0 - C_t}{C_0} \times 100 \tag{3}$$

where ŋ represents the degradation efficiency and C_0 and C_t are initial concentration and concentration of MB dye at time t. The evolution of ŋ during the experiment time is plotted in Fig. 6c. Both samples show their highest photocatalytic activity in the first 30 mins interval and the rate of purification experiences diminution over time. Photocatalytic activity of pure and nanowhisker-covered samples presents the 34% degradation with the nanostructured surface against the 17% degradation in the presence of reference sample which yields in two-fold decontamination after 30 minutes. This result corroborates the efficiency of TiO_2 nanowhiskers for MB dyes decomposition which can be related to their higher surface to volume ratio of photocatalytic sites. The other aspect of higher degradation rate in S-doped nanowhisker samples can be dealt with the role of sulfur doping. As the XPS analysis confirms, for the concurrent possible cationic and anionic nature of doping, the doping of sulfur atoms can bring oxygen and titanium vacancy states which results in electron-hole recombination suppression and further higher photocatalytic activity[70].

The degradation rate of solutions experiences variations after the first 30 minutes of the experiment. Figure 6d plots temporal MB dye concentration variation (C_t/C_0) over the test period. As seen, the degradation mechanism differs in the decontamination process of two catalysts. The reference TiO_2 exhibits linear characteristics over the experiment time which could be related to two possible mechanisms: (1) the diffusion-limiting regime governing the photocatalytic interaction between adsorbate and adsorbent and the apparent physisorption of dyes on the surface; (2) the adsorption of contaminants playing chemisorption properties but the deficiency of reactive sites limits the chemical adsorption process. Despite consistent slope found in the degradation rate of reference TiO_2, the nanostructured surface exhibits a non-linear feature which specifies different catalytic kinetics governing their cleansing process. The temporal concentration changes depict that TiO_2 nanostructures and MB dyes have interaction on the sample's surface and contaminants have made chemisorption on TiO_2

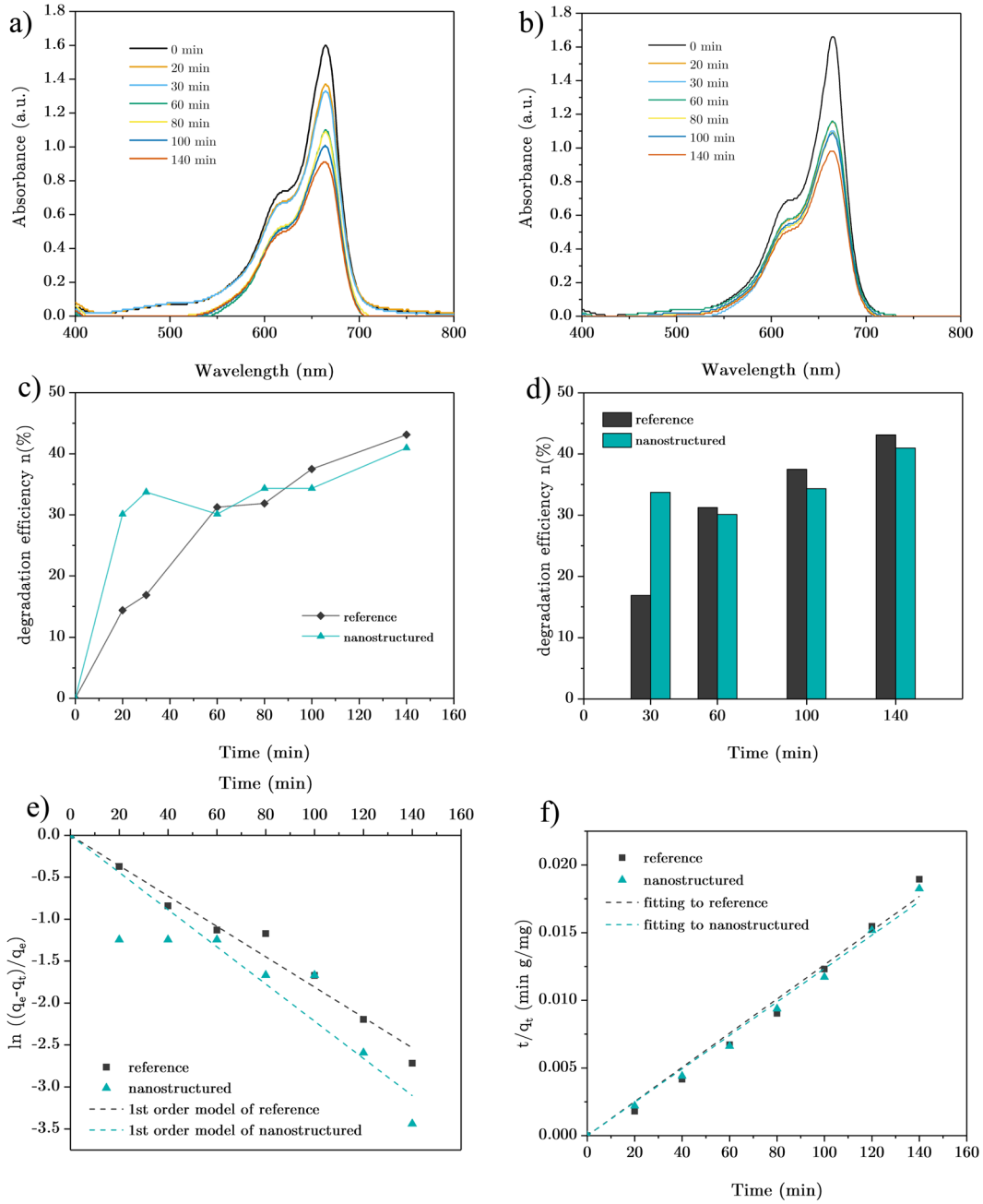

Figure 6. The photocatalytic behavior of the reference and nanostructured samples. (**a**) The absorption spectrum of 10ppm MB aqueous solution photo-degraded with reference sample TiO_2 catalyst, (**b**) absorption spectra of solution in the presence of TiO_2 nanowhisker sample, (**c**) temporal changes of photo-degradation efficiency during photocatalytic experiment, (**d**) bar chart of degradation efficiency variation in two photocatalytic processes, (**e**) adsorption kinetics of reference and nanostructured TiO_2 samples modeled with pseudo first-order equation, (**f**) pseudo second-order fitting of the decontamination process.

nanowhiskers. This adsorption has not resulted in the saturation of photocatalytic surface which could suppress the photo-degradation process[71], but the lower rate of adsorption has affected the efficiency of nanostructured samples in degrading MB solution.

To better understand various mechanisms participating in the rate-controlling of photo-degradation process kinetic models can be employed. Due to different degradation characteristics derived from two samples, the heterogeneous photocatalytic processes have been modeled with both first-order and second-order kinetics. For this purpose, the Lagergren pseudo-first-order equation (Eq. 4)[72] and also Ho's pseudo-second-order formula (Eq. 5)[73] are used for modeling the characteristics of both samples.

Rate Law	Photocatalytic sample	Rate Constant (K)	COD (R^2)
Lagergren's pseudo first order	Reference	0.0181 (min^{-1})	0.975
	Nanostructured	0.0222 (min^{-1})	0.835
Ho's pseudo second order	Reference	1.262×10^{-4} ($g\ min^{-1}\ mg^{-1}$)	0.984
	Nanostructured	1.235×10^{-4} ($g\ min^{-1}\ mg^{-1}$)	0.991

Table 1. Rate constants and the coefficient of determination (COD) calculated for two samples with the aid of pseudo-first and second-order models.

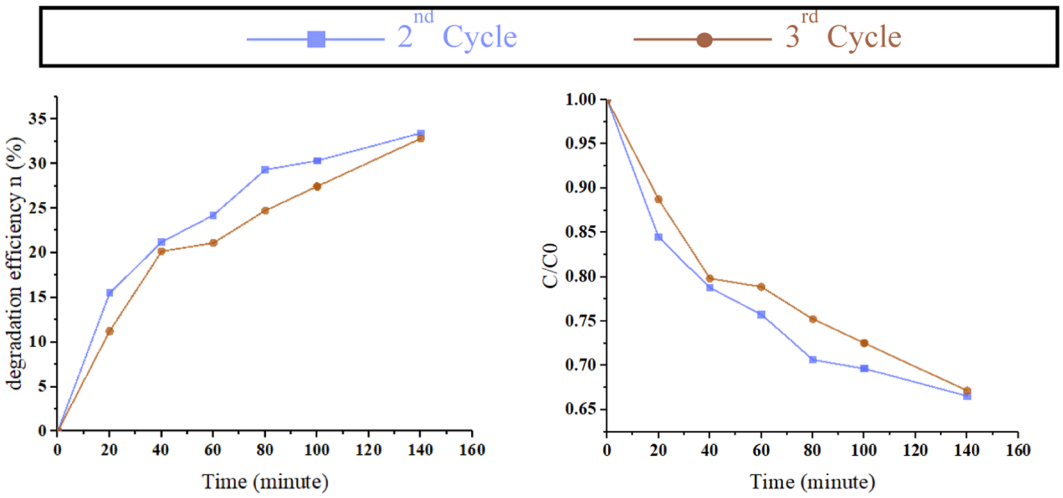

Figure 7. The second and third stages of cycling experiment for the degradation of MB in the presence of photocatalyst. In both cases, a monotonic rise in the degradation efficiency is observed, although the efficiency shows a slight reduction at the third cycle.

$$ln\left(\frac{q_e - q_t}{q_e}\right) = k_1 t \tag{4}$$

$$\frac{t}{q_t} = \frac{1}{k_2 q_e^2} + \frac{t}{q_e} \tag{5}$$

where q_e and q_t denote the adsorption capacity (mg/g) at equilibrium with respect to the time of the experiment (t). k_1 (min^{-1}) and k_2 (g/mg. min^{-1}) represent the rate constants of pseudo-first and second-order formalisms, respectively. Figure 6e depicts the pseudo-first-order fitting of the photo-degradation process of two catalysts by plotting temporal changes of $\ln((q_e - q_t)/q_e)$ versus time. The quality of fitting and the rate constant "k_1" are extracted for each sample and presented in Table 1. The coefficient of determination gained from the nanostructured TiO_2 plot, reveals the inability of first-order kinetics to fully interpret the governing mechanism for the photocatalytic degradation of MB in the presence of nanowhiskers. Nonetheless, the correlation of reference sample photo-degradation and pseudo-first-order model exhibits a good interpretation. Finally, part (f) represents the pseudo-second-order modeling of processes by plotting t/q_t over the experiment time period. The coefficient of determination for two fittings displays a distinct improvement in the case of nanostructured catalyst expressing that the MB dyes experience chemisorption on nanowhiskers, yielding in a descending scheme of photodegradation rate after 30 minutes of the process. On the other hand, the relative variation of determination of coefficient in the reference sample shows a minor enhancement. Through fitting of pseudo-first and second-order models to the reference sample, it is deduced that the adsorption of contaminants on the reference catalyst surface might have a slight chemical bonding, but it cannot make dominancy to limit the photocatalytic degradation process.

As stability is an important parameter in the photocatalyst efficiency, the photocatalyst has undergone a cycle test. The result of further cycles on the photocatalyst sample is presented in Fig. 7. These experiments were performed with the same recipe which has been conducted to the nanostructured sample (10 mL aqueous MB solution, 160 Watts, 365 nm UV lamp irradiation in 140 min duration).

The cycle experiment reveals that the photodegradation of MB in the presence of photocatalyst decreased from about 40 percent degradation after 140 min in the first cycle presented in Fig. 6c to 33.5% in the second cycle and 33% in the third one. On the other hand, this trend of decrements exhibits a saturation in the possible efficiency gaining from the presented photocatalyst sample.

Summary and Conclusion

Single-crystalline sulfur-doped TiO_2 nano-whiskers were grown in a dual-zone CVD furnace. The growth was monitored by means of loading/unloading mechanism being installed on the CVD reactor. The synthesis of TiO_2 nano-whiskers was held in a sulfur-rich environment, leading to sulfur doping of nanostructures. The elemental analysis by EDX along with Raman spectroscopy revealed that the growth substrate for nano-whiskers formed in a layered stack of TiS_2 and TiO_2 films. This layered structure is a result of the sequential growth method, where the surface-featured titanium substrate experienced a sulfurization and subsequent oxidation step. Our investigations show that nanowhiskers are formed TiS_2 seeds through oxidation and cooling steps.

The observed enhancements in the growth of nanostructures are believed to be due to the introduction of chlorine agents. The reaction between Ti substrate and chlorine gas provides the appropriate medium for the local growth of TiS_2 sheets leading to confined $TiO_{2-x}S_x$ sheets. On the other hand, the SEM and Raman spectroscopy findings state that the faceted growth of TiO_2 nanowhiskers can be retained from the formation of anatase TiO_2 layers and the chlorine gas can act as a prohibitory agent in the anatase to rutile phase transformation. Consequently, the chlorine agent plays an effective role in the growth of TiO_2 nanostructures. The evolution of TiS_2 layers and their transformation into TiO_2 films and further nanosheets growth would eventually lead to S-doped heterostructures. The EDX mapping and line scanning of TiO_2 nano-whiskers showed the presence of Sulfur doping. Also, transmission electron microscopy shows the ultrathin nature of synthesized nanosheets and the fact that the TiO_2 whiskers are formed in a layered nature, proposing that such nano-whiskers are 2D sheets made of sulfur-doped titanium dioxide.

The photocatalytic behavior of TiO_2 substrates covered with sulfur-doped nanosheets was studied by the so-called aqueous Methylene blue (MB) decontamination photocatalytic process. These nanostructured samples showed a two-fold enhancement in the photocatalytic activity in comparison with the reference TiO_2 substrate during the first interval of 30 mins. The interpretation of degradation of MB dyes in the presence of nanostructures had been achieved through second-order fitting and pseudo-second-order kinetic modeling. These results express possible chemisorption of dyestuff on the TiO_2 nanowhiskers during the photocatalytic procedure. We believe much higher photocatalytic degradation efficiency can be achieved by increasing the TiO_2 nanosheet surface participating in the photocatalytic procedure.

Received: 25 July 2019; Accepted: 4 November 2019;
Published online: 29 November 2019

References

1. Vequizo, J. J. M. *et al*. Trapping-Induced Enhancement of Photocatalytic Activity on Brookite TiO_2 Powders: Comparison with Anatase and Rutile TiO_2 Powders. *ACS Catal.* **7**(no. 4), 2644–2651 (2017).
2. O'Regan, B. & Grätzel, M. A low-cost, high-efficiency solar cell based on dye-sensitized colloidal TiO_2 films. *Nature* **353**, 737–740 (1991).
3. Dudefoi, W., Moniz, K., Allen-Vercoe, E., Ropers, M.-H. & Walker, V. K. Impact of food grade and nano-TiO_2 particles on a human intestinal community. *Food and Chemical Toxicology* **106**, 242–249 (2017).
4. Jokinen, M. *et al*. Influence of sol and surface properties on *in vitro* bioactivity of sol-gel-derived TiO_2 and TiO_2-SiO_2 films deposited by dip-coating method. *Journal of Biomedical Materials Research banner* **42**(no. 2), 295–302 (1998).
5. Song, Y.-Y., Schmidt-Stein, F., Bauer, S. & Schmuki, P. Amphiphilic TiO_2 Nanotube Arrays: An Actively Controllable Drug Delivery System. *Journal of American Chemical Society* **131**(no. 12), 4230–4232 (2009).
6. Wang, Z. *et al*. Transferable and Flexible Nanorod-Assembled TiO_2 Cloths for Dye-Sensitized Solar Cells, Photodetectors, and Photocatalysts. *ACS Nano* **5**(no. 10), 8412–8419 (2011).
7. Shaban, M., Ashraf, A. & Abukhadra, M. TiO_2 Nanoribbons/Carbon Nanotubes Composite with Enhanced Photocatalytic Activity; Fabrication, Characterization, and Application. *Scientific Reports* **8**(no. 1), 781 (2018).
8. Armstrong Dr., A. R., Armstrong, G., Canales Dr, J. & Bruce Prof, P. G. TiO_2-B Nanowires. *angewandte chemie* **43**(no. 17), 2286–2288 (2004).
9. Altomare, M., Truong Nguyen, N., Hejazi, S. & Schmuki, P. A Cocatalytic Electron-Transfer Cascade Site-Selectively Placed on TiO_2 Nanotubes Yields Enhanced Photocatalytic H_2 Evolution. *Advanced Functional Materials* **28**(no. 2), 1704259 (2017).
10. Leng, M., Chen, Y. & Xue, J. Synthesis of TiO_2 nanosheets via an exfoliation route assisted by a surfactant. *Nanoscale* **6**(no. 15), 8531–8534 (2014).
11. Javed, S., Islam, M. & Mujahid, M. Synthesis and characterization of TiO_2 quantum dots by sol gel reflux condensation method. *Ceramics International* **45**(no. 2), 2676–2679 (2019).
12. Wu, H. B., Hng, H. H. & Lou, X. W. Direct Synthesis of Anatase TiO_2 Nanowires with Enhanced Photocatalytic Activity. *Advanced Materials* **24**(no. 19), 2567–2571 (2012).
13. Zhao, Y., Hoivik, N., Akram, M. N. & Wang, K. Study of plasmonics induced optical absorption enhancement of Au embedded in titanium dioxide nanohole arrays. *Optical Materials Express* **7**(no. 8), 2871–2879 (2017).
14. Liu, G. *et al*. Titanium Dioxide Crystals with Tailored Facets. *Chemical Reviews* **114**(no. 19), 9559–9612 (2014).
15. Ye, L. *et al*. Synthesis of anatase TiO_2 nanocrystals with {101}, {001} or {010} single facets of 90% level exposure and liquid-phase photocatalytic reduction and oxidation activity orders. *J. Mater. Chem. A* **1**(no. 35), 10532–10537 (2013).
16. Lazzeri, M., Vittadini, A. & Selloni, A. Structure and energetics of stoichiometric TiO_2 Anatase surfaces. *Phys. Rev. B* **63**(no. 15), 155409 (2002).
17. Duminica, F.-D., Maury, F. & Hausbrand, R. Growth of TiO_2 thin films by AP-MOCVD on stainless steel substrates for photocatalytic applications. *Surface and Coatings Technology* **201**(no. 22–23), 9304–9308 (2007).
18. Evans, P., Pemble, M. E. & Sheel, D. W. Precursor-Directed Control of Crystalline Type in Atmospheric Pressure CVD Growth of TiO_2 on Stainless Steel. *Chem. Mater.* **18**(no. 24), 5750–5755 (2006).
19. Chambers, S. A. *et al*. Epitaxial growth and properties of MBE-grown ferromagnetic Co-doped TiO_2 anatase films on $SrTiO_3$(001) and $LaAlO_3$(001). *Thin Solid Films* **418**(no. 2), 197–210 (2002).
20. Yang, H. G. *et al*. Solvothermal Synthesis and Photoreactivity of Anatase TiO_2 Nanosheets with Dominant {001} Facets. *J. Am. Chem. Soc.* **131**(no. 11), 4078–4083 (2009).
21. Yin, H. *et al*. Hydrothermal synthesis of nanosized anatase and rutile TiO_2 using amorphous phase TiO_2. *J. Mater. Chem.* **11**(no. 6), 1694–1703 (2001).
22. Guo, W. *et al*. Rectangular Bunched Rutile TiO_2 Nanorod Arrays Grown on Carbon Fiber for Dye-Sensitized Solar Cells. *J. Am. Chem. Soc.* **134**(no. 9), 4437–4441 (2012).

23. Yang, H. G. *et al*. Anatase TiO_2 single crystals with a large percentage of reactive facets. *Nature* **453**, 638–641 (2008).
24. Kotsyubynsky, V. O. *et al*. The Effect of Sulphate Anions on the Ultrafine Titania Nucleation. *Nanoscale Research Letters* **12**, 369 (2017).
25. Hanaor, D. A. H. & Sorrell, C. C. Review of the anatase to rutile phase transformation. *Journal of Materials Science* **46**(no. 4), 855–874 (2011).
26. Yu, J. *et al*. Preparation, characterization and photocatalytic activity of *in situ* Fe-doped TiO_2 thin films. *Thin Solid Films* **496**(no. 2), 273–280 (2006).
27. Chen, X. & Burda, C. The Electronic Origin of the Visible-Light Absorption Properties of C-, N- and S-Doped TiO_2 Nanomaterials. *J. Am. Chem. Soc.* **130**(no. 15), 5018–5019 (2008).
28. Li, N. *et al*. High quality sulfur-doped titanium dioxide nanocatalysts with visible light photocatalytic activity from non-hydrolytic thermolysis synthesis. *Inorg. Chem. Front.* **1**, 521–525 (2014).
29. Li, W. *et al*. A Review of Recent Applications of Ion Beam Techniques on Nanomaterial Surface Modification: Design of Nanostructures and Energy Harvesting. *Small* **15**(no. 31), 1901820 (2019).
30. Song, X. *et al*. The "Midas Touch" Transformation of TiO_2 Nanowire Arrays during Visible Light Photoelectrochemical Performance by Carbon/Nitrogen Coimplantation. *Advanced Energy Materials* **8**(no. 20), 1800165 (2018).
31. Umebayashi, T., Yamaki, T., Itoh, H. & Asai, K. Band gap narrowing of titanium dioxide by sulfur doping. *Appl. Phys. Lett.* **81**, 454 (2002).
32. Yang, G., Yan, Z. & Xiao, T. Low-temperature solvothermal synthesis of visible-light-responsive S-doped TiO_2 nanocrystal. *Applied Surface Science* **258**(no. 8), 4016–4022 (2012).
33. Ho, W., Yu, J. C. & Lee, S. Low-temperature hydrothermal synthesis of S-doped TiO_2 with visible light photocatalytic activity. *Journal of Solid State Chemistry* **179**(no. 4), 1171–1176 (2006).
34. Han, C. *et al*. The effect of solvent in the sol–gel synthesis of visible light-activated, sulfur-doped TiO_2 nanostructured porous films for water treatment. *Catalysis Today* **224**(no. 1), 132–139 (2014).
35. Cravanzola, S., Cesano, F., Gaziano, F. & Scarano, D. Sulfur-Doped TiO_2: Structure and Surface Properties. *Catalysts* **7**(no. 7), 214 (2017).
36. Jing, H. *et al*. Synthesis of TiO_2 nanosheet photocatalysts from exfoliation of TiS_2 and hydrothermal treatment. *Journal of Materials Research*, pp. 1–9 (2018).
37. Gao, Z. *et al*. *In Situ*-Generated Volatile Precursor for CVD Growth of a Semimetallic 2D Dichalcogenid. *ACS Appl. Mater. Interfaces* **10**(no. 40), 34401–34408 (2018).
38. Johnson, W. H., Nelson, R. A. & Prosen, E. Heat of Formation of Titanium Tetrachloride. *Journal of Research of the National Bureau of Standards* **62**(no. 1), 49–52 (1959).
39. Zhang, Q. H., Gao, L. & Guo, J. Effects of calcination on the photocatalytic properties of nanosized TiO_2 powders prepared by $TiCl_4$ hydrolysis. *Applied Catalysis B: Environmental* **26**(no. 3), 207–215 (2000).
40. Chianelli, R. R. & Dines, M. B. Low-temperature solution preparation of Group 4B, 5B and 6B transition-metal dichalcogenides. *Inorganic Chemistry* **17**(no. 10), 2758–2762 (1978).
41. Palgrave, R. G. & Parkin, I. P. Chemical vapour deposition of titanium chalcogenides and pnictides and tungsten oxide thin films. *New Journal of Chemistry* **no. 4**, 505–514 (2006).
42. Chang, H. & Schleich, D. TiS_2 and TiS_3 thin films prepared by MOCVD. *Journal of Solid State Chemistry* **100**(no. 1), 62–70 (1992).
43. Balachandran, U. & Eror, N. Raman Spectra of Titanium Dioxide. *Journal of Solid State Chemistry* **42**, 276–282 (1982).
44. Ohsaka, T., Izumi, F. & Fujiki, Y. Raman spectrum of anatase, TiO_2. *journal of raman spectroscopy* **7**(no. 6), 321–324 (1978).
45. Picquenard, E., El Jaroudi, O. & Corset, J. Resonance Raman spectra of the S3 molecule in sulphur vapour. *Journal of Raman Spectroscopy* **24**(no. 1), 11–19 (1993).
46. Tompsett, G. A. *et al*. The Raman spectrum of brookite, TiO_2 (Pbca, Z = 8). *Journal of Raman Spectroscopy* **26**(no. 1), 57–62 (1995).
47. Clegg, I. M., Everall, N. J., King, B., Melvin, H. & Norton, C. On-Line Analysis Using Raman Spectroscopy for Process Control during the Manufacture of Titanium Dioxide. *Applied Spectroscopy* **55**(no. 9), 1138–1150 (2001).
48. Castrejón-Sánchez, V., Camps, E. & Camacho-López, M. Quantification of phase content in TiO_2 thin films by Raman spectroscopy. *Superficies y vacío* **27**(no. 3), 88–92 (2014).
49. Shastri, A., Datye, A. & Schwank, J. Influence of chlorine on the surface area and morphology of TiO_2. *Applied Catalysis* **14**, 119–131 (1985).
50. Huckaba, A. J. *et al*. Low-Cost TiS2 as Hole-Transport Material for Perovskite Solar Cells. *Small Methods* **1**(no. 10), 1700250 (2017).
51. Abu Bakar, S. & Ribeiro, C. A comparative run for visible-light-driven photocatalytic activity of anionic and cationic S-doped TiO_2 photocatalysts: A case study of possible sulfur doping through chemical protocol. *Journal of Molecular Catalysis A: Chemical* **421**, 1–15 (2016).
52. Han, C. *et al*. Innovative visible light-activated sulfur doped TiO_2 films for water treatment. *Applied Catalysis B: Environmental* **107**(no. 1–2), 77–87 (2011).
53. Li, H., Zhang, X., Huo, Y. & Zhu, J. Supercritical Preparation of a Highly Active S-Doped TiO_2 Photocatalyst for Methylene Blue Mineralization. *Environ. Sci. Technol.* **41**(no. 12), 4410–4414 (2007).
54. Yu, J. C. *et al*. Efficient Visible-Light-Induced Photocatalytic Disinfection on Sulfur-Doped Nanocrystalline Titania. *Environ. Sci. Technol.* **39**(no. 4), 1175–1179 (2005).
55. Gardy, J., Hassanpour, A., Lai, X. & Ahmed, M. H. Synthesis of $Ti(SO_4)O$ solid acid nano-catalyst and its application for biodiesel production from used cooking oil. *Applied Catalysis A: General* **527**, 81–95 (2016).
56. Hawkins, C. & Whittaker-Brooks, L. Controlling Sulfur Vacancies in TiS_{2-x} Cathode Insertion Hosts via the Conversion of TiS_3 Nanobelts for Energy Storage Applications. *ACS Appl. Nano Mater.* **1**(no. 2), 851–859 (2018).
57. Ohno, T. *et al*. Preparation of S-doped TiO_2 photocatalysts and their photocatalytic activities under visible light. *Applied Catalysis A: General* **265**(no. 1), 115–121 (2004).
58. Znad, H. & Kawase, Y. Synthesis and characterization of S-doped Degussa P25 with application in decolorization of Orange II dye as a model substrate. *Journal of Molecular Catalysis A: Chemical* **314**(no. 1–2), 55–62 (2009).
59. Wang, X., Li, Z., Shi, J. & Yu, Y. One-Dimensional Titanium Dioxide Nanomaterials: Nanowires, Nanorods, and Nanobelts. *Chemical Revews* **114**(no. 19), 9346–9384 (2014).
60. Yuanzhi, L., Nam-Hee, L., Jae, S. S., Eun Gu, L. & Sun-Jae, K. Synthesis and photocatalytic properties of nano bi-crystalline titania of anatase and brookite by hydrolyzing $TiOCl_2$ aqueous solution at low temperatures. *Research on Chemical Intermediates* **31**(no. 4-6), 309–318 (2005).
61. Li, X. *et al*. SnS_2/TiO_2 Nanohybrids Chemically Bonded on Nitrogen-doped Graphene for Lithium-Sulfur Batteries: Synergy of Vacancy Defects and Heterostructure. *Nanoscale* **10**(no. 33), 15505–15512 (2018).
62. Slinkˌ W. E. & DeGroot, P. B. Vanadium-titanium oxide catalysts for oxidation of butene to acetic acid. *Journal of Catalysis* **68**(no. 2), 423–432 (1981).
63. Huang, P. *et al*. Room Temperature and Aqueous Solution-Processed 2D TiS_2 as Electron Transport Layer for Highly Efficient and Stable Planar n-i-p Perovskite Solar Cells. *ACS Appl. Mater. Interfaces* **10**(no. 17), 14796–14802 (2018).
64. Niu, X. *et al*. Hydrothermal synthesis and formation mechanism of the anatase nanocrystals with co-exposed highenergy {001}, {010} and [111]-facets for enhanced photocatalytic performance†. *RSC Advances* **7**(no. 40), 24616–24627 (2017).

65. Hawkins, C. G. & Whittaker-Brooks, L. Vertically Oriented TiS_{2-x} Nanobelt Arrays as Binder– and Carbon– Free Intercalation Electrodes for Li– and Na– based Energy Storage Devices. *Journal of Materials Chemistry A* **6**(no. 44), 21949–21960 (2018).
66. Akcakoca, E. & Aysegul Korlu, K. Textile Wastewater Treatment, Intechopen (2016).
67. Salehi, M., Hashemipour, H. & Mirzaee, M. Experimental Study of Influencing Factors and Kinetics in Catalytic Removal of Methylene Blue with TiO_2 Nanopowder. *American Journal of Environmental Engineering* **2**(no. 1), 1–7 (2012).
68. Zhang, T. *et al*. Photooxidative N-demethylation of methylene blue in aqueous TiO_2 dispersions under UV irradiation. *Journal of Photochemistry and Photobiology A: Chemistry* **140**(no. 2), 163–172 (2001).
69. Yao, J. & Wang, C. Decolorization of Methylene Blue with Sol via UV Irradiation Photocatalytic Degradation. *International Journal of Photoenergy* **2010**, 6 (2010).
70. Devi, L. & Kavitha, R. Enhanced photocatalytic activity of sulfur doped TiO_2 for the decomposition of phenol: A new insight into the bulk and surface modification. *Materials Chemistry and Physics* **143**(no. 3), 1300–1308 (2014).
71. San Román, E. A., Navio, J. A. & Litter, M. I. Photocatalysis with Fe/TiO_2 Semiconductors and TiO_2 Sensitized by Phthalocyanines. *Journal of Advanced Oxidation Technologies* **3**(no. 3), 261–269 (1998).
72. Lagergren, S. About The Theory of So-Called Adsorption of Soluble Substances. *Kungliga Svenska Vetenskapsakademiens Handlingar* **24**(no. 4), 1–39 (1898).
73. Ho, Y. & McKay, G. Pseudo-second order model for sorption processes. *Process Biochemistry* **34**, 451–465 (1999).

Author contributions

S. Ahmad Etghani: This author is a PhD candidate and has a major contribution in designing the experimental setup as well as characterizing and writing the manuscript. Apart from physical characterization, the setup for photocatalysis experiment has been devised by him. His contribution has been very critical in this work. Ehsan Ansari: This author has major contribution in devising the setup, especially the cool and vent part which has led to the formation of TiS_2 films. In addition, Ehsan has carried out most of the SEM analysis for this work. He has also been working in the writing and correction of the manuscript. Shams Mohajerzadeh: This author is the supervisor of this work. His contribution lays in the initial idea for the experimental setup and guidance of the work towards the formation of 2D nano-structures. The main fabrication setup, i.e. the customized CVD reactor has been his suggestion. Apart from analyzing the data, he has a major contribution in writing and modifying this hectic manuscript.

Competing interests

The authors declare no competing interests.

Additional information

Supplementary information is available for this paper at https://doi.org/10.1038/s41598-019-53651-y.

Correspondence and requests for materials should be addressed to S.M.

Reprints and permissions information is available at www.nature.com/reprints.

Publisher's note Springer Nature remains neutral with regard to jurisdictional claims in published maps and institutional affiliations.